RSC
Applied Interfaces

ROYAL SOCIETY
OF CHEMISTRY

PAPER

View Article Online
View Journal | View Issue

Check for updates

Cite this: *RSC Appl. Interfaces*, 2025, **2**, 150

On the characterization and performance of highly dispersed TiO_2 nanoparticles onto BEA zeolite in the continuous gas-phase photooxidation of ethylene†

Ricardo Ferreira,[ab] Sergio Morales-Torres,[b] Luisa M. Pastrana-Martinez,[b] Francisco J. Maldonado-Hódar,[b] João Paulo Lourenço,[ac] João Miguel Silva,[ad] Isabel M. João,[de] Maria Filipa Ribeiro[a] and Auguste Fernandes*[a]

Received 13th August 2024,
Accepted 8th October 2024

DOI: 10.1039/d4lf00286e

rsc.li/RSCApplInter

Two series of TiO_2-based zeolite composites (BEA structures) were prepared by employing a sol–gel method using two different synthesis approaches, *i.e.*, acidic and basic media. Different photocatalytic composites obtained with increasing amounts of TiO_2 (10–50 wt%) were thoroughly characterized and subsequently tested in the photooxidation of ethylene in a continuous gas-phase system. Results showed that sol–gel experimental conditions had a significant effect on the final properties of the samples, as photocatalytic composites obtained under basic conditions showed better TiO_2 dispersion and interaction with the BEA support than their counterparts prepared in an acidic medium. The same photocatalysts showed high performance in ethylene photooxidation, demonstrating complete mineralization and results comparable to or even better than those of the bulk TiO_2 material.

Introduction

Ethylene (C_2H_4) is a natural hormone found in fruits and vegetables that induces their growth, ripening and senescence.[1] Apart from accelerating fruit maturation, ethylene can lead to fruit spoilage, reducing shelf life and causing huge losses worldwide each year, with wastes estimated for this sector as much as 20–60%.[2] Because the global demand for fruits is increasing, concerns about food quality and food waste minimization are rising in population priorities. For these reasons, ethylene removal in fruit transportation and cold storage chambers has been the subject of several studies.[1,3,4] Many different (chemical and/or physical) methods can be used for ethylene elimination,[5] for example, the use of chemical inhibitors (*e.g.*, 1-MCP), chemical oxidation with $KMnO_4$, adsorption methods and different advanced oxidation processes (AOPs).[5,6] Among all the available methods and technologies applied in the food storage industry, the ethylene photooxidation method appears a very promising opportunity.

Although many different photocatalytic materials can be potentially employed for such a purpose (one can cite nanostructured ZnO,[7] for example), TiO_2 photocatalyst is, by far the most common and popular semiconductor studied for photocatalytic purposes, probably because of their unique properties such as chemical inertness, high stability, low cost and, undoubtedly, efficient photoactivity under UV light.[8] TiO_2 photocatalysts have received much attention from the food industry. Indeed, TiO_2-based alternative postharvest technologies have demonstrated a strong potential in ethylene removal through photodegradation, especially for the storage of fresh products and/or manufacturing of food-active packaging.[5,9,10] However, successful ethylene photooxidation technologies, already mature, are still a challenging task, in part because of the need to find a highly efficient photocatalyst material. One interesting solution is the coupling of photocatalytic oxidation with another ethylene control method, such as ventilation or adsorption.[5] Preparing composites based on TiO_2 and a zeolite-based adsorbent seems to be a promising solution for obtaining highly efficient ethylene removal *via* photooxidation. In fact, zeolite materials present many advantages over other adsorbent materials. They can play an important role in increasing ethylene concentration, thus improving the reaction rate of the photocatalytic oxidation process.[5] However, owing to their capacity to disperse well the

---

[a] *Centro de Química Estrutural, Institute of Molecular Sciences, Instituto Superior Técnico, Universidade de Lisboa, Lisboa, Portugal. E-mail: auguste.fernandes@tecnico.ulisboa.pt*
[b] *Nanomaterials and Sustainable Chemicals Technologies, Department of Inorganic Chemistry, Faculty of Science, University of Granada, Granada, Spain*
[c] *Faculdade de Ciências e Tecnologia, Universidade do Algarve, Faro, Portugal*
[d] *Instituto Superior de Engenharia de Lisboa, Lisboa, Portugal*
[e] *CEGIST, Instituto Superior Técnico, Universidade de Lisboa, Lisboa, Portugal*

† Electronic supplementary information (ESI) available. See DOI: https://doi.org/10.1039/d4lf00286e

active phase, zeolites are commonly used as supports for metals and metal oxide supports.[11] In particular, many studies have focused on the incorporation of titanium into zeolite and silicate materials. Depending on the synthesis methods used to introduce Ti, two different Ti-based zeolite materials can be obtained: Ti-containing zeolites/silicates and TiO_2-zeolite composites. In the first case, Ti is essentially incorporated within the zeolite structure, replacing Si and thus adopting tetrahedral coordination.[12] In the second case, zeolite is used as a support to obtain highly dispersed TiO_2 nanoparticles at the surface of the zeolite.[13–15] The ultimate goal consists of preparing a TiO_2-based zeolite composite with highly active TiO_2 species, which is at least more active than bulk TiO_2 materials.[12,15] BEA structure has prevailed among all the different zeolite supports that have been studied as potential support of TiO_2 for several reasons: a) the high surface area and also the presence of silanol defects enable the incorporation of TiO_2 as isolated tetrahedral Ti(IV) species;[16,17] b) the good adsorption properties that enhance the photodegradation efficiency of zeolite-supported TiO_2;[18] c) the possibility to transfer the excited electrons of TiO_2 to the zeolite support can lead to a decrease in the e^-/hole recombination rate and the subsequent improvement of the composite photocatalytic efficiency.[14,18] In fact, many photocatalytic reactions, such as ketonisation,[17] epoxidation[16] and photooxidation of volatile organic compounds (VOCs), in both liquid and gas-phase systems,[14,18–20] have been studied with BEA-based TiO_2 composites.

In this work, we show the use of BEA-based TiO_2 composites in the photooxidation of ethylene in a gas-phase system. TiO_2/BEA zeolite composites were prepared using a sol–gel method, with two different alcohols (2-propanol and ethanol) and different TiO_2 concentrations (10–50 wt%) in the final composites. The photocatalysts were tested under two types of irradiation: UV-vis and UVA-vis lights. The results demonstrated the presence of different TiO_2 species, well dispersed on the surface of the zeolite support. The resulting BEA-TiO_2 composites showed highly efficient photocatalytic activity in ethylene photooxidation.

Results and discussion

Characterization of the TiO_2 bulk samples

Fig. 1 shows the PXRD patterns (left) and the N_2 isotherms (right) for the three bulk TiO_2 samples used for this

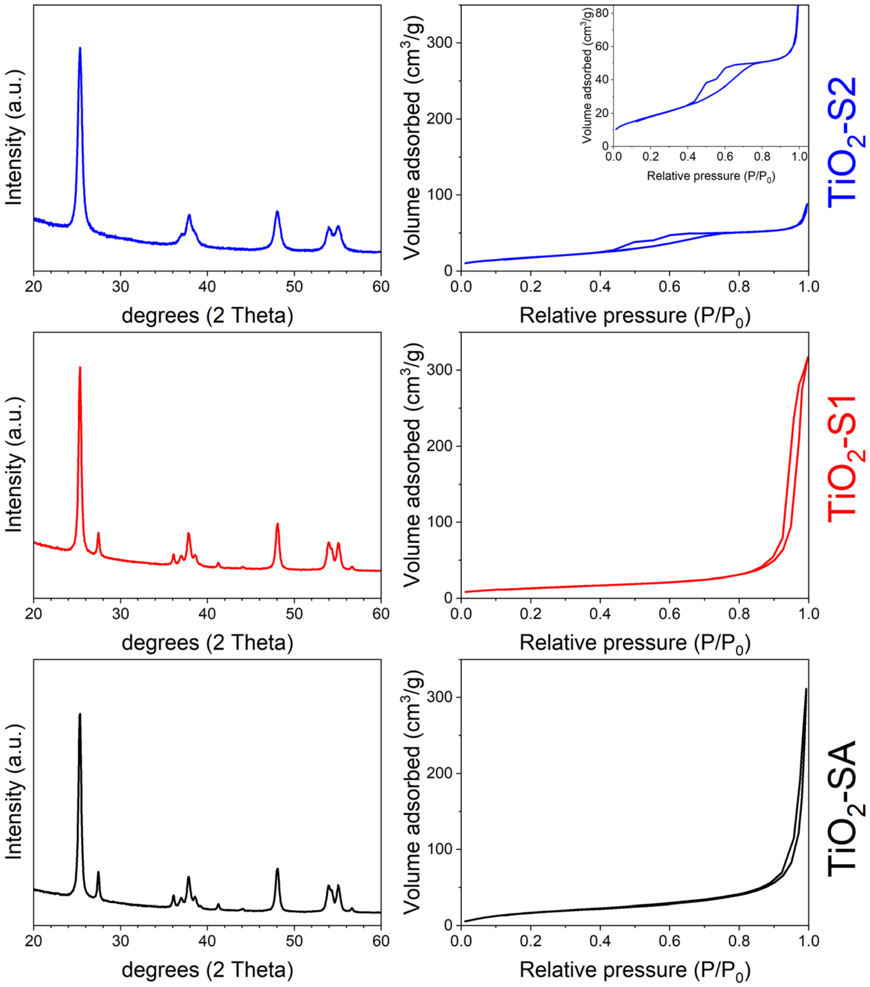

Fig. 1 (Left) PXRD patterns and (right) N_2 isotherms (at 77 K) of bulk TiO_2 samples: TiO_2-SA (black), TiO_2-S1 (red) and TiO_2-S2 (blue). Inset: details of the TiO_2-S2 isotherm.

comparative study (the respective pore size distribution (PSD) curves are presented in Fig. S1, ESI†). TiO_2-SA sample consists of a mixture of anatase and rutile phases (main peaks at 25.33 and 27.47°, respectively), with peaks rather broad, indicating very small crystallites. The TiO_2-S1 sample shows the same behavior as the TiO_2-SA one, meaning that the samples are very similar in terms of anatase/rutile weight ratio and crystallite size. This result agrees well with the study of Molea *et al.*,[21] who showed that acidic pH conditions during TiO_2 sol–gel preparation give a mixture of anatase and rutile, while basic conditions favor the anatase phase. The sol–gel process might be driven essentially by the pH of the solution.[22] Under acidic conditions, deoxolation does not occur during nucleation; instead, olation leads to the growth of linear chains that condense by oxolation to form a rutile phase. Under basic conditions, deoxolation occurs prior to olation and condensation can proceed along apical directions, with the formation of anatase structure. In fact, the TiO_2-S2 sample synthesized under basic sol–gel conditions corresponds to a pure anatase phase (absence of the main rutile peak at 27.47° in 2θ). This sample also presents broader peaks, revealing even smaller particles. This is also well in line with the work of Bahar *et al.*,[23] who demonstrated that ethanol solvent favored the formation of small TiO_2 particles while propanol favored larger TiO_2 ones. All these observations are supported by the quantitative PXRD analysis performed, as presented in Table 1. TiO_2-SA and TiO_2-S1 samples present the same amount of anatase and rutile (87 and 13 wt%, respectively) and crystallite size (18–19 nm for the anatase phase). These results also agree well with common values found in the literature for P25-like TiO_2 materials.[24] However, the pure anatase TiO_2-S2 sample shows smaller crystallites (about 11 nm).

The textural properties obtained for the bulk TiO_2 samples are in line with previous comments. TiO_2-SA and TiO_2-S1 samples present a type II isotherm with a high uptake at high P/P_0, typical of nanoparticle aggregates, with a significant interparticular mesopore volume. Interestingly, the TiO_2-S1 sample shows hysteresis at a lower P/P_0 value when compared with TiO_2-SA, indicating that mesopores are smaller in size (33 against 65 nm). Moreover, both samples show a non-negligible surface area of about 50–70 $m^2\ g^{-1}$, typical for nanosized TiO_2 materials, *e.g.* P25.[25] In contrast, TiO_2-S2 presents a type IV isotherm and a hysteresis in a range of 0.4–0.8 P/P_0 (mesopores of about 5 nm), reflecting the presence of much smaller TiO_2 particles. This latter sample also presents a surface area comparable to the TiO_2-SA reference (66 $m^2\ g^{-1}$). The SEM images of both sol–gel TiO_2 samples corroborate the previous comments (see ESI† Fig. S2). The TiO_2-S1 sample shows large and loosely aggregated particles, while TiO_2-S2 presents smaller particles that easily aggregate to form coral-like nanostructures. Interestingly, this morphology was also found by Bahramian[26] who used a very similar sol–gel recipe to synthesize their nanostructured TiO_2 films (ethanol and aqueous acid solution). This difference in particle morphology also explains well the difference in pore sizes for the two samples: larger interparticular mesopores for TiO_2-S1 (*ca.* 33 nm) and smaller mesopores for the TiO_2-S2 sample (*ca.* 5 nm). Although it is difficult to determine the average size of the particles for both bulk TiO_2 samples, these SEM images fairly agree with the crystallite's sizes determined from PXRD measurements (about 20 and 10 nm for TiO_2-S1 and TiO_2-S2 samples, respectively).

Table 1 Structural and textural properties of bulk TiO_2 materials

	XRD analysis[a]		Textural parameters		
Sample	Anatase	Rutile	V_{total}[b]	S_{BET}[c]	Pore size[d]
TiO_2-SA	87 (19)	13 (30)	0.48	67	65
TiO_2-S1	88 (18)	12 (28)	0.49	48	33
TiO_2-S2	100 (11)	—	0.14	66	5

[a] Quantitative phase analysis (wt%) and crystallites size (nm). [b] ($cm^3\ g^{-1}$). [c] ($m^2\ g^{-1}$). [d] From the maxima of BJH curves, desorption branch (nm).

Fig. 2 presents the absorption spectra obtained for the 3 different TiO_2 samples. In all cases, an intense and broad band below 400 nm can be observed, with maxima at *ca.* 240 and 300–330 nm. All the spectra agree well with those reported for bulk TiO_2 materials. In particular, the band at 275–330 nm is well known to be the characteristic of bulk TiO_2 (anatase or rutile).[27,28] Interestingly, TiO_2-SA and TiO_2-S1 samples, which present similar crystallite sizes and the same anatase/rutile ratio also present a similar UV absorption profile, with a shoulder at about 310 nm. However, the pure anatase TiO_2-S2 sample presents a different profile, with the most intense band appearing at a higher wavelength (*ca.* 330 nm).

Characterization of the TiO_2-BEA composites

Structural and textural characterization. The various TiO_2-BEA composites were first characterized by powder X-ray

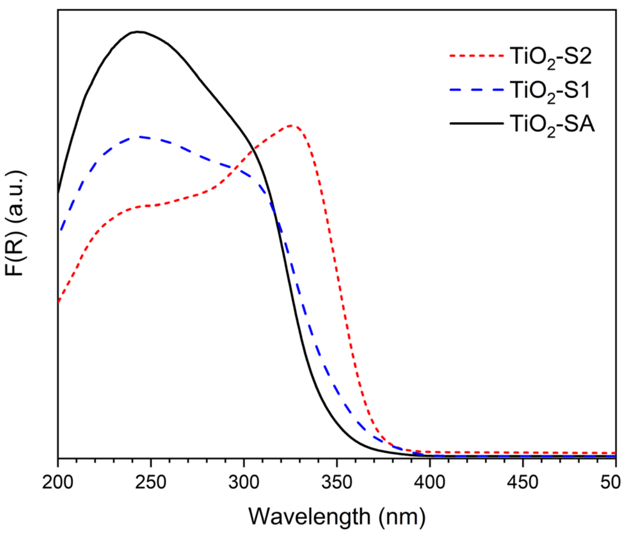

Fig. 2 UV-vis DRS spectra of bulk TiO_2 samples: TiO_2-SA (black), TiO_2-S1 (blue) and TiO_2-S2 (red).

diffraction. Fig. S3† shows a comparison between the raw support (BEA zeolite) and composites. As can be observed, all the composites show typical broad lines of BEA zeolite. However, for both series, the intensity of the peaks corresponding to the BEA phase decreases with the increasing amount of TiO_2 in the final composites. Although some destruction of the zeolite support cannot be completely ruled out, the decrease in the BEA peak intensity might essentially be due to a dilution effect. Furthermore, peaks from the anatase and/or rutile phases can be observed in some samples. To better understand the effect of the TiO_2 presence, each composite pattern was compared with the H-BEA pattern (with both patterns normalized relative to the peak at about 21–22° in 2θ). The results are presented in Fig. 3 for both series. For a better comparison, diffraction lines of anatase (COD-9009086) and rutile (COD-907432) phases are also shown.

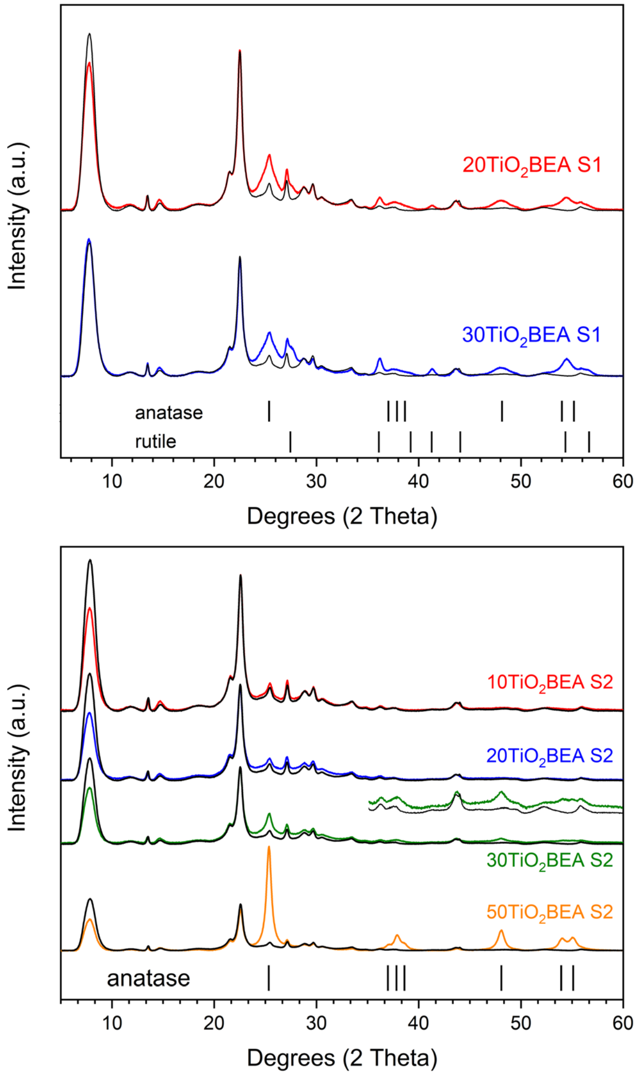

Fig. 3 PXRD patterns of the different composite materials: (top) S1 series and (bottom) S2 series. For a better comparison, for each sample, the H-BEA pattern is compared.

Regarding the S1 composite series, independently of the TiO_2 amount, an increase in the intensity in the 24–28° region is observed and indicates the presence of both anatase and rutile phases in the final composites. This is confirmed by an increase in intensity at about 38, 48 and 56° (in 2θ). However, for the S2 composite series, the results are quite different. Below 30 wt% TiO_2, no substantial differences are observed between the BEA zeolite and composite patterns. However, for TiO_2 loading of 30 wt% or higher, clear differences between composite and raw BEA patterns can be observed, especially for the 50TiO_2-BEA S2 sample. In this case, the XRD pattern is dominated by peaks corresponding to the anatase phase. Moreover, if diffraction peaks from the rutile phase can be easily identified for the series S1 composites, this phase is not observed for the S2 series samples. However, if both anatase and rutile phases can be identified for the S1 series at a relatively low TiO_2 loading (20 wt%), this is not the case for the S2 series, where a higher amount of TiO_2 is necessary to observe an anatase phase in the final composite patterns. Similar to what happens with the bulk TiO_2 samples, the sol–gel preparation of composites under basic conditions seems to favour the presence of anatase only, whereas, under acidic conditions, both anatase and rutile phases appear.

The textural properties of the different composites are presented in Table 2. Fig. 4 shows the pore size distribution (PSD) curves obtained for the different materials, while Fig. S4 (in ESI†) illustrates the nitrogen isotherms of the respective materials. The H-BEA sample presents an isotherm that corresponds to type I at low relative pressure but also an important uptake for $P/P_0 > 0.4$ and a subsequent H3 hysteresis, corresponding to the interparticle voids into and between aggregates. Consequently, the H-BEA sample presents a very large external surface area (205 $m^2 g^{-1}$) and a large mesopore volume. This is in agreement with the SEM images of H-BEA support, showing aggregates of very small particles (about 20–30 nm, see Fig. 5)[29] (0.78 $cm^3 g^{-1}$). The different composites present essentially the same isotherm profile as the H-BEA support but with a systematic decrease in nitrogen uptake because of the presence of TiO_2 (see Fig. S4†). This decrease in nitrogen adsorption for both series implies a decrease in both micropore and mesopore volumes, especially for the S2 series.

However, for that later series, the external surface area increases when compared with pristine H-BEA support and S1 series composites. The PSD curves of the different samples show a decrease in the larger mesopores (20–30 nm) and a concomitant increase in the smaller mesopores (2–3 nm), especially for the samples of the S2 series. This observation could be explained by the fact that the amount of zeolite support decreases with the amount of TiO_2; consequently, the interparticular mesoporosity derived from the zeolite nanoparticle aggregates decreases.

The SEM images of the different composites are shown in Fig. 5 together with the raw H-BEA support. As stated previously, zeolite support consists of aggregates of *ca.* 30 nm

Table 2 Acidic and textural properties of TiO_2/BEA zeolite composites

	Acidity properties			Textural properties			
Sample	B sites[a,b]	L sites[a,b]	B (350/150)[c]	V_{micro}[d]	V_{meso}[e]	S_{ext}[f]	S_{BET}[g]
H-BEA	553 (553)	335 (335)	0.49	0.17 (100)	0.78	205	627
20TiO_2-BEA S1	320 (399)	296 (370)	0.48	0.13 (96)	0.50	211	541
30TiO_2-BEA S1	185 (265)	208 (297)	0.50	0.11 (92)	0.58	214	477
10TiO_2-BEA S2	416 (462)	368 (409)	0.42	0.14 (92)	0.77	241	575
20TiO_2-BEA S2	365 (456)	360 (450)	0.37	0.12 (88)	0.54	238	516
30TiO_2-BEA S2	320 (457)	290 (415)	0.38	0.09 (76)	0.55	314	522
50TiO_2-BEA S2	223 (446)	246 (492)	0.38	0.06 (71)	0.42	208	349
TiO_2-S2	0	108	—	0	0.14	—	66

[a] Amount of Brønsted (B) and Lewis (L) acid sites (μmol) per gram of the composite determined at 150 °C. [b] In () amount of B and L acid sites (μmol) per g of zeolite determined at 150 °C. [c] B ratio = Brønsted acid sites at 350 °C/Brønsted acid sites at 150 °C. [d] $cm^3\ g^{-1}$ (percentage of V_{micro} considering only the amount of zeolite in the final composite material). [e] $V_{meso} = V_{total} - V_{micro}$ ($cm^3\ g^{-1}$). [f] From *t*-plot ($m^2\ g^{-1}$). [g] SBET calculated in the P/P0 range of 0.05–0.3.

in size particles. Both 10TiO_2-BEA S2 and 20TiO_2-BEA S2 samples present an identical morphology and are very similar to the H-BEA sample (results not shown for the 10TiO_2-BEA S2 sample for the sake of simplicity). For those samples that present low TiO_2 loading, no significant difference can be observed with BEA support, *i.e.*, TiO_2 particles can hardly be observed. However, with the increase in the TiO_2 loading (30–50 wt%), the coral-like morphology, characteristic of TiO_2 nanoparticle aggregates (TiO_2-S2 sample), is now visible, together with aggregates of larger particles coming from the BEA support (see Fig. 5).

The presence of these coral-like TiO_2 aggregates might explain the presence of the hysteresis in the isotherms of the S2 series composites at about 0.5–0.8 P/P_0 (see ESI,† Fig. S4, right) and the consequent increase, in the PSD curves in the contribution of the smaller pores (2–3 nm). One can note that the same hysteresis is also observed for bulk TiO_2-S2 samples (*cf.* Fig. 1). However, for the TiO_2-based S1 series, the results

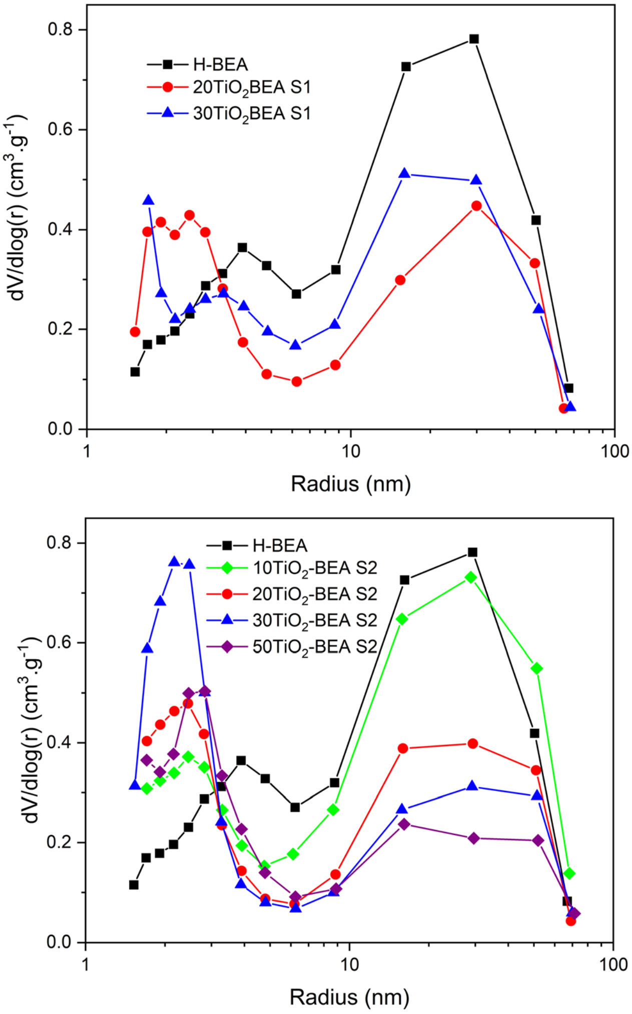

Fig. 4 Pore size distribution curves (BJH, desorption branch) of TiO_2-BEA composites: (top) S1 series and (bottom) S2 series.

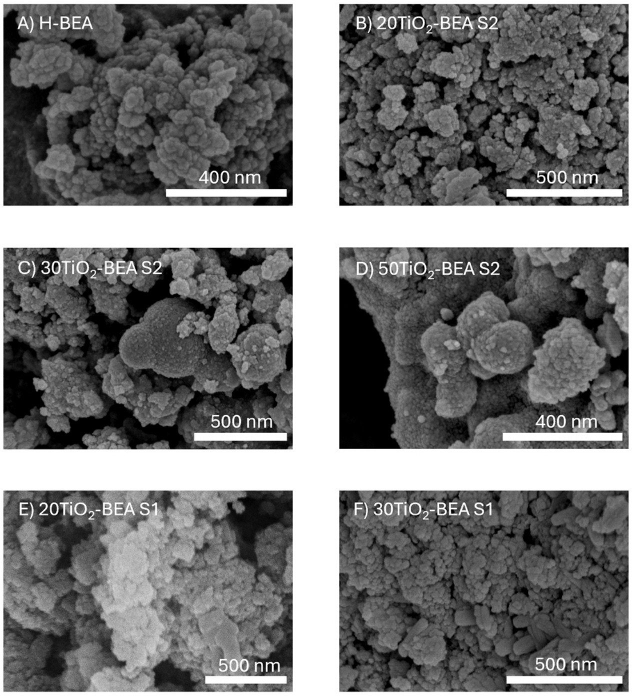

Fig. 5 SEM images of the different composites: A) H-BEA, B) 20TiO_2-BEA S2, C) 30TiO_2-BEA S2, D) 50TiO_2-BEA S2, E) 20TiO_2-BEA S1 and F) 30TiO_2-BEA S1 samples.

are quite different. Here, large particles with a distinct morphology, contrasting with the aggregates formed by the zeolite particles, can be observed for the 20TiO_2-BEA S1 sample. These large platelet-like particles might correspond to the anatase/rutile phases detected in the XRD patterns of the respective samples. These isolated TiO_2 nanoparticles are even more evident for the 30TiO_2-BEA S1 sample.

As observed previously, the analysis of the XRD patterns of the different composites reveals that the intensity of the zeolite peaks gradually decreases with the increase in the TiO_2 loading, whether other peaks (from TiO_2 phases) appear or not. In particular, for the S2 series samples presenting a low TiO_2 content (10–20 wt%), no extra peak is observed although the diffraction lines of the BEA support decrease substantially. This result suggests that TiO_2 species might interact strongly with the zeolite surface without crystallization of a separated bulk crystalline TiO_2 phase, as no extra phase can also be observed in the SEM images.

To obtain a more detailed insight into this S2 series samples (10–20 wt% TiO_2), STEM analysis was performed. The results are shown in ESI† (Fig. S5) for both 10TiO_2-BEA S2 and 20TiO_2-BEA S2 samples. EDS analyses were crucial for understanding the distribution of titanium within the zeolite matrix. In the composite with 10 wt% TiO_2, Ti is dispersed within the zeolite structure in smaller amounts than that observed for the 20 wt% TiO_2 sample, as expected. No TiO_2 nanocrystals are visible in the 10TiO_2-BEA S2 sample. On the contrary, in the 20TiO_2-BEA S2 sample, TiO_2 nanocrystals of approximately 5 nm in size are observed (Fig. S6(f)†). The observed TiO_2 nanocrystal was further investigated, and the HAADF-STEM image in the inset of Fig. S6(f)† clearly shows the Ti atom columns, with a measured lattice spacing of 3.8 Å, corresponding to the (100) and (010) atomic planes of the TiO_2 anatase crystalline phase. Observed along the [001] zone axis, the angles between (100) and (010) measured in the FFT image are 90°, which is consistent with the theoretical value reported for pure crystalline TiO_2 anatase (ICSD 9852). These STEM results also help in explaining the textural differences between the two composites series. In the case of the S2 samples, the presence of well-dispersed Ti atoms together with the presence of very small TiO_2 nanoparticles strongly attached at the surface of the BEA support might cause the blockage of some micropores. Indeed, the decrease in the micropore volume is more significant for the S2 series than for the S1 series. The lower decrease in microporosity for these later samples should be justified by the weaker interaction between TiO_2 nanoparticles and the BEA support.

Spectroscopic characterization of the TiO_2-BEA composites

To obtain a better insight into the exact interaction between TiO_2 species and BEA zeolite support, FTIR, UV-vis DRS, Raman and XPS experiments were performed. Fig. 6 shows the different FTIR reflectance spectra obtained for the composites and compared with the bulk TiO_2-S1 oxide. The two other TiO_2 bulk samples (spectra not shown) present the same features as TiO_2-S1, a spectrum essentially dominated by a very large and intense band below 1000 cm^{-1} corresponding to Ti–O stretching.[30] H-BEA support presents typical structural bands from BEA zeolite at 1230, 1070 and 790 cm^{-1}.[20] The intense band at about 1070 cm^{-1} corresponds to the asymmetric T–O–T stretching mode and is normally related to internal tetrahedra vibrations (T–O–T, T = Si, Al), while the shoulder at 1230 cm^{-1} corresponds to external tetrahedra linkages, which are more sensitive to the zeolite topology and/or the building units.[31] The spectroscopic feature of this shoulder has been shown to change with the Si/Al ratio, zeolite structure amorphization,

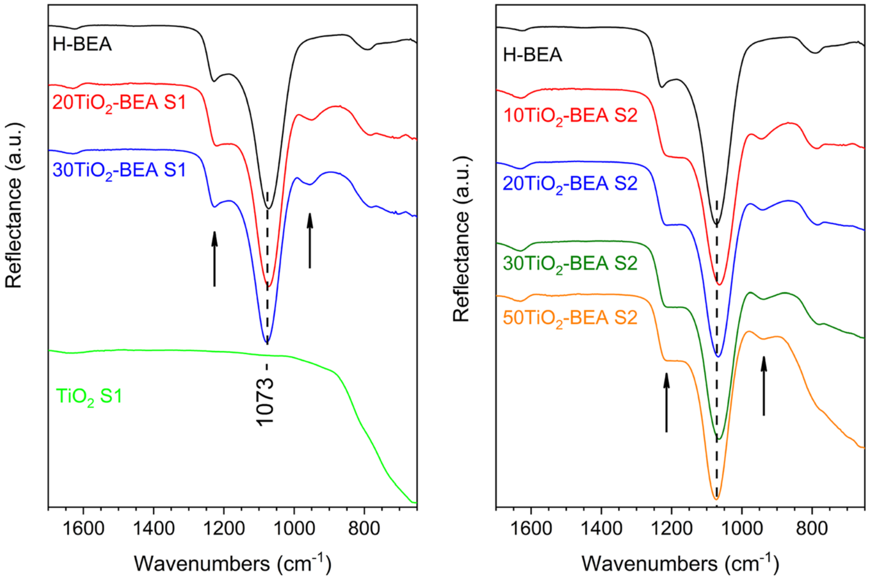

Fig. 6 FTIR spectra of the different composite materials (ATR mode): (left), S1 series, and (right) S2 series (the arrows in both figures depict the bands at about 1230 and 950 cm^{-1}).

etc. When looking at the spectra of the composites, one can observe important differences when compared with the BEA sample. For all the composites, a band at about 950 cm^{-1} is observed for all the samples, except for the pristine BEA sample, which seems to be more prominent for the 10TiO_2-BEA S2 sample. Additionally, for this sample, the strong band corresponding to asymmetric T–O–T stretching (1063 cm^{-1}) is shifted when compared with all the other samples (1073 cm^{-1}). The baseline also starts to tilt down below 900 cm^{-1}.

These two observations can be easily understood by considering the presence of various TiO_2 species in the final composites. The band at ~950 cm^{-1} has already been observed for TiO_2-Y zeolite[32] and TiO_2-modified MCM-41[33] systems, among others. It is generally related to either framework TiO_4 or Ti interacting with TO_4 species (T = Si or Al) and has been used as an indication of the presence of Ti–O–Si bonds in the respective materials[20,27,32,33] or T–O–T bonds perturbed by Ti(VI) species.[34] However, the baseline decrease indicates the presence of extra-framework Ti(IV) species in the form of bulk TiO_2. Finally, for series S2 samples, the shoulder initially visible at 1230 cm^{-1} seems to vanish, probably indicating a stronger interaction between TiO_2 species and the zeolite support surface for this series of composites.

Table 2 presents the acidity properties of the different samples determined using pyridine adsorption followed by FTIR spectroscopy. The results concerning the bulk TiO_2-S2 sample are also presented for comparison: the sample only presents Lewis acid sites, *i.e.*, no Brønsted acid sites are detected for this sample. The results obtained show an important decrease in the Brønsted acid site concentration with the amount of TiO_2 in the final composites. In particular, the decrease in the Brønsted acidity seems to be more pronounced for the S1 series than for the S2 series, even if the support dilution is considered (Table 2). Interestingly, the Brønsted acidity strength, *i.e.*, the ratio between the concentration of Brønsted acid sites at 350 and 150 °C (determined from pyridine desorption with temperature and followed by FTIR) is similar between the raw BEA zeolite and the S1 series samples (about 0.49) but decreases substantially for S2 series samples (0.38) (Table 2).

This result could be understood if one considers a change in the electronegativity of the zeolite surface for this S2 series due to the presence of strongly interacting TiO_x species, considering that Ti is less electronegative than Al and Si (1.54 against 1.61 and 1.90, respectively). Another explanation might be that the interaction between TiO_2 nanoparticles and the BEA surface could generate additional Brønsted acid sites. This has been observed by Doolin *et al.*[35] who studied the acidity properties of titania-silica mixed oxides. They first concluded that both silica and titania oxides, taken separately, do not present any Brønsted acidity. Then, they verified that by combining the two oxides, Brønsted acidity could be generated, in a similar way to the silica-alumina system. They also concluded that the Brønsted acid sites generated are weaker than those found for YH zeolite material. In our case, the presence of weaker Brønsted acid sites could indicate a strong interaction between TiO_2 nanoparticles and the BEA surface, resulting in the formation of these new Brønsted acid sites. However, the evolution of the Lewis acidity is not straightforward. All the spectra corresponding to the composite materials show an extra peak at about 1445 cm^{-1} together with the usual peak at 1455 cm^{-1} corresponding to pyridine adsorbed onto classical Al-based Lewis acid sites (see Fig. S6 in ESI†). According to El-Roz *et al.*, the former peak corresponds to pyridine adsorbed onto a TiO_2 Lewis acid site.[20] Odenbrand and coworkers,[36,37] who studied similar TiO_2–SiO_2 chemical systems, observed the existence of, not one, but two types of Lewis sites associated with the presence of Ti in TiO_2–SiO_2 systems, tetrahedrally coordinated Ti atoms in addition to the coordinately unsaturated octahedral Ti ions. These former tetrahedral sites were thought to be considerably stronger Lewis acid sites than their octahedral counterparts. In our case, as a decrease in the Lewis acidity strength is observed when TiO_2 is present, one can speculate that these weak Lewis acid sites (see Fig. S6†), newly formed in the presence of TiO_2, are associated with Ti species presenting octahedral coordination. The estimation of the amount of Lewis sites derived exclusively from TiO_2 species present in the composites might be rather difficult. Nevertheless, one can observe that samples from the S2 series present a similar or even higher amount of total Lewis acid sites than BEA support alone (see Table 2) despite a lower micropore volume. Moreover, the S1 series samples present a similar Lewis acidity and a similar micropore volume. We can then conclude that, in the S2 samples, the highly dispersed TiO_2 species and/or nanoparticles might contribute to a higher amount of Lewis acid sites.

The UV-vis DRS spectra of the different composites are presented in Fig. 7. For the S1 series, the absorption spectra resemble the one of the bulk TiO_2-S1 sample. The band at about 300–330 nm, characteristic of bulk TiO_2 (anatase or rutile),[27,28] is already present in both spectra, meaning that composites are essentially made of a mixture (zeolite/bulk TiO_2) although with some TiO_2 species interacting more strongly with the support (*vide infra*). However, for the S2 samples series, the behavior is quite different. For the S2 sample series with a low TiO_2 content (10 and 20 wt%), the UV-vis DRS spectra are quite different from the bulk TiO_2 S2 sample, as they do not present any band at 310–330 nm, but rather a band centered at 255 nm. This significant blue shift when compared with raw TiO_2 materials is commonly interpreted in the literature as the size quantization effect,[28,38,39] where the band maximum suffers a blue shift with the decrease in the TiO_2 particle size. This decrease in particle size might also be responsible for higher light scattering, and decreasing absorbance cannot be ruled out. In our case, this decrease in wavelength could also be explained by the presence of poorly polymerized TiO_2 species, interacting strongly with the zeolite surface, as revealed by XRD and FTIR results. The spectra of 30TiO_2-BEA S2 and 50TiO_2-BEA S2 samples, however, present a component at about 305 nm (a clear shoulder is observed for the later sample). Here, the TiO_2 content is probably enough for

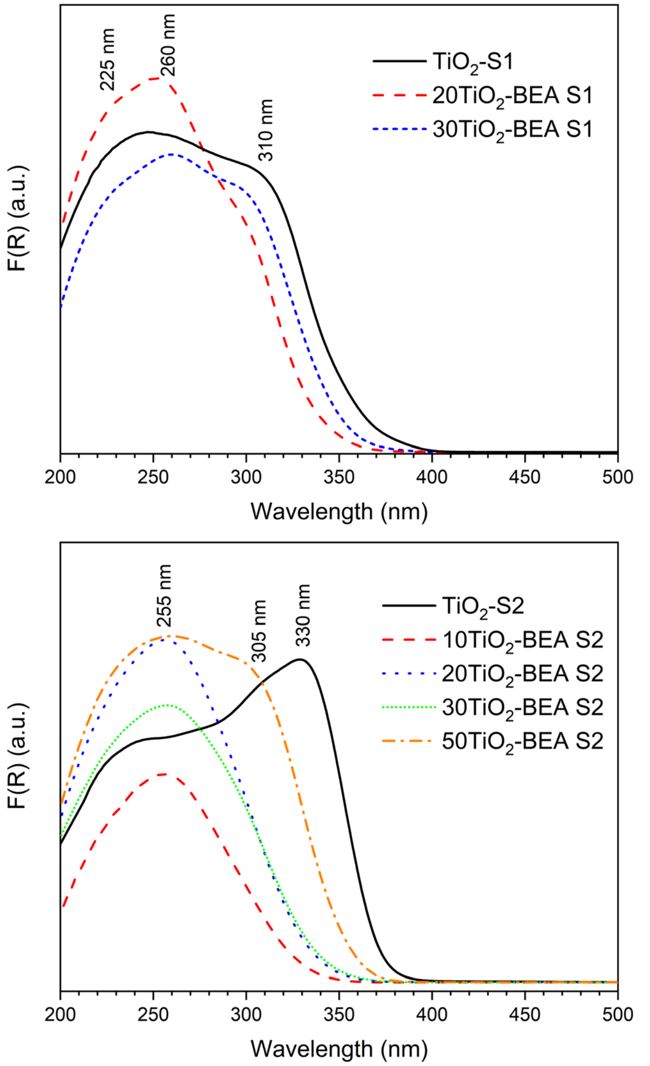

Fig. 7 UV-vis DRS spectra of series S1 (top) and S2 (bottom) composite materials.

the formation of a free bulk TiO_2 phase, with almost no interaction with zeolite support, as confirmed by the SEM images (see Fig. 5). The band gap values, calculated from the Tauc plot curves, are presented in Table S1 (see ESI†). TiO_2-SA was used as a reference (band gap of 3.33 eV, in agreement with the literature[24]). As expected from the UV-vis DRS spectra obtained, most of the composites have a band gap value between 3.2 and 3.5 eV. Interestingly, all the composites have a BG value higher than their respective bulk TiO_2 references, meaning that all the composites present a blue-shift absorption when compared with respective references.

Several studies focusing on TiO_2-based zeolite composites (especially BEA support) have shown the presence of TiO_2 species other than anatase-like TiO_2 oxide, *i.e.*, mononuclear TiO_2, TiO_2 nanoclusters, extra-framework Ti species, *etc.*, present at the surface of the zeolite support.[16,40–42] In particular, the interesting work by Klaas *et al.*[28] gives important insights concerning the definition of these Ti-based species: a) polymeric, anatase-like TiO_2 species are characterized by an intense band above 300 nm (typically 310–330 nm); b) the absorption energies increase with a decrease in the coordination number. This is the reason why Ti(IV) species in a tetrahedral environment (TS-1, TS-2 materials) are characterized by an absorption band at about 200–210 nm; c) the absorption coefficient of cations usually rises by 1 or 2 orders if the coordination changes from centrosymmetry to noncentrosymmetry, or in other words, from ideal to strongly distorted octahedral or to lower coordination, meaning that low coordination/distorted Ti species present a strong absorption at a relatively low wavelength, even though these species are in low concentration in the material.

Following the above statements, we can more specifically define the different TiO_x species that coexist simultaneously in our various TiO_2-BEA composites. For a low TiO_2 content, these TiO_2 species might be essentially penta and/or hexacoordinated, either isolated or in oligomeric form, as they are characterized by absorption bands ranging from 225 to 255–270 nm. These TiO_x species might also be coordinatively saturated because no changes occurred in the respective absorption spectra after dehydration (results not shown). We can also differentiate the S1 series samples from the S2 series samples. In fact, for the S1 series samples, anatase-like (highly polymerized) TiO_2 species dominate because of the presence of a characteristic band above 300 nm. In the case of the S2 series samples, TiO_x species, possibly penta/hexacoordinated, poorly oligomerized, and interacting strongly with the zeolite support might prevail. We will see, in the subsequent paragraphs, that both Raman and XPS spectroscopies results support the above findings.

Fig. 8 shows the Raman spectra of the different samples. For the S1 series samples, the Raman spectra are very similar and show two sets of lines at 153, 402, 522 and 642 cm^{-1}, and 440 and 610 cm^{-1} which, according to the literature, are characteristics of anatase and rutile, respectively.[21] In both cases, the fluorescence from the zeolite support is hidden by the strong signal from the respective TiO_2 and appears in the spectrum background. However, the Raman spectra of the S2 series sample are dominated by a strong background usually observed for zeolite-based materials, which is normally explained by the fluorescence of organic species adsorbed onto the zeolite support and/or the presence of Fe present in the zeolite framework.[43] Furthermore, for samples presenting a low TiO_2 content, no peak characteristics of TiO_2 can be observed. Nonetheless, the presence of TiO_2 is confirmed for the samples with a higher TiO_2 content (30 and 50 wt%), with a peak observed at about 144 cm^{-1} for both samples, despite the intense background generated by fluorescence. In the case of the 50TiO_2-BEA S2 sample, three additional peaks with a very low intensity can also be observed at 402, 520 and 640 cm^{-1}, confirming the presence of an anatase-like TiO_2 phase. These Raman results clearly corroborate our prior conclusions. If the anatase and rutile phases seem to crystallize separately from the zeolite support for the S1 series samples, the same is not observed for the S2 series, where TiO_2 might interact more

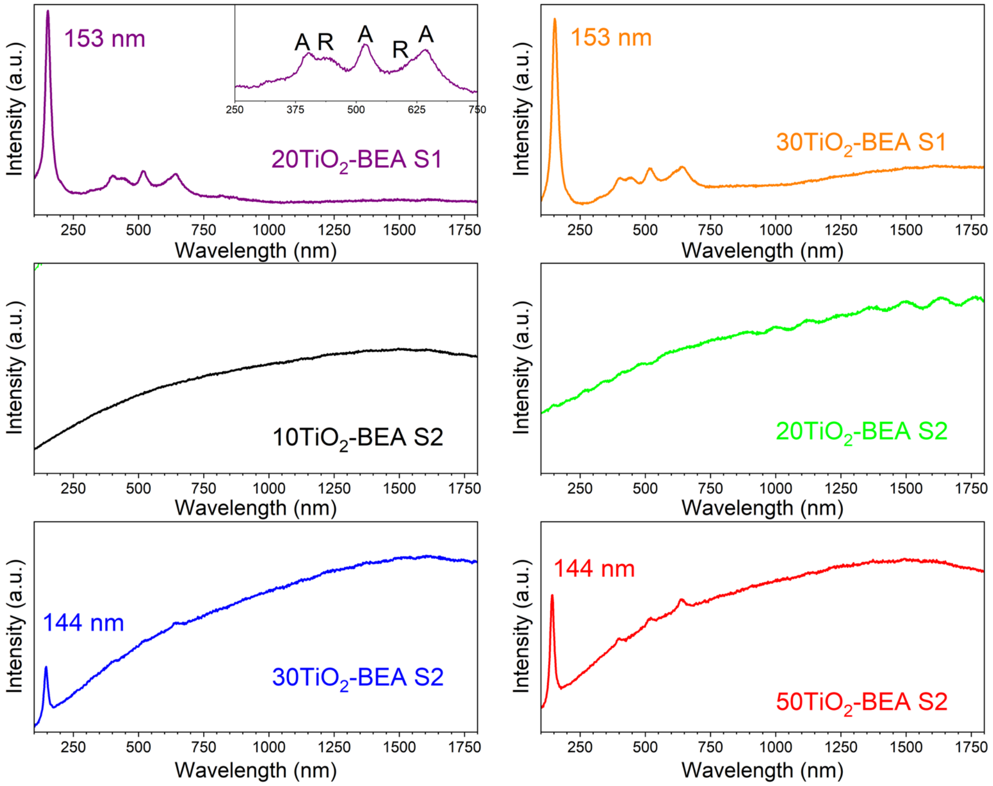

Fig. 8 Raman spectra of the different BEA-based composites (532 nm laser) (inset: details of the spectrum in the region 250–750 nm).

strongly with the BEA support. This results in a loss of the centrosymmetry for the TiO$_x$ units, hence making the respective vibrations Raman inactive.[28]

The Ti2p and O1s XPS spectra of the S2 series composites are presented in Fig. 9. For the 10TiO$_2$-BEA S2 sample, the Ti2p region is dominated by a doublet at 466.3 and 460.6 eV corresponding to Ti2p$_{1/2}$ and Ti2p$_{3/2}$ components, respectively. These values are very different from those of bulk TiO$_2$-SA, which shows peaks at 464.2 and 458.5 eV, typical values for polymeric TiO$_2$ oxide (see ESI,† Fig. S5). These two-component peaks at higher energy are characteristic of Ti^{4+} in a tetrahedral environment/coordination, *e.g.*, in many titanium-based silicate materials (TS-1,[44] TS-2[45]). However, according to Camblor and

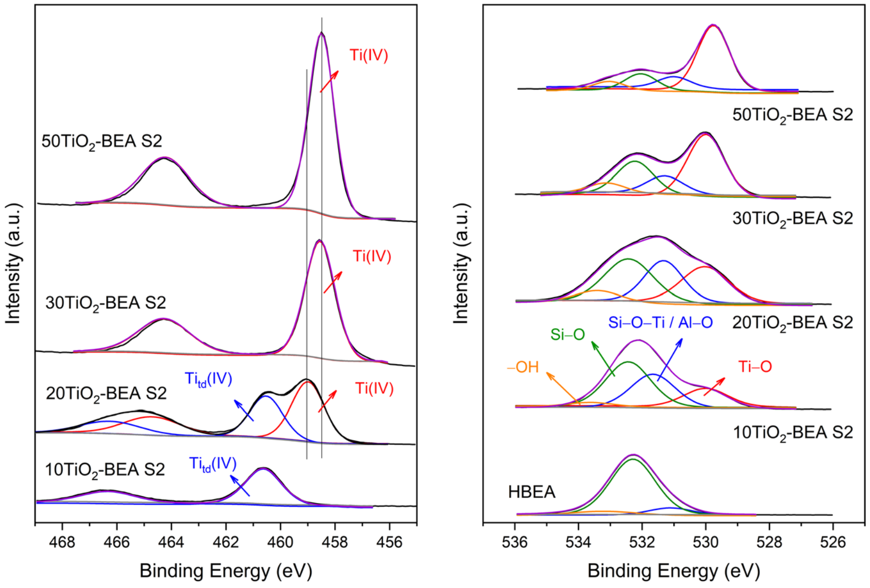

Fig. 9 XPS spectra of S2 series samples. Left: Ti2p core-level region; right side: O1s region.

coworkers,[46–48] this doublet high in energy does not necessarily mean that Ti(IV) species are present with a tetrahedral coordination but might also account for Ti species in octahedral sites. Indeed, these authors studied two natural titanosilicate minerals, ramsayite and benitoite, with distinct Ti species features. In the case of ramsayite, the distorted octahedral TiO_6 units share two edges and one independent corner with other TiO_6 octahedra (forming TiO_6 chains) and corners with SiO_4 tetrahedra; for benitoite, the symmetric TiO_6 octahedra are isolated in the silica matrix, *i.e.*, each TiO_6 unit is only surrounded by SiO_4 neighbors in the first shell.

The authors concluded that the presence of SiO_4 units in the respective minerals causes a shift in the respective Ti2p signal to a higher energy. In their case, they observed a BE $Ti2p_{3/2}$ peak at 459.8 and 460.2 eV for ramsayite and benitoite, respectively. In our case, the $Ti2p_{3/2}$ contribution of the $10TiO_2$-BEA S2 sample is at 460.6 eV. Because this sample presents a maximum in the absorption spectrum at 250–260 nm and no changes are observed in the absorption spectrum after dehydration, we tentatively attribute this XPS signal to distorted octahedral Ti species, strongly interacting with the surface of the zeolite and probably highly dispersed, that is, poorly oligomerized (see STEM and Raman results). With the increase in Ti content in the composite ($20TiO_2$-BEA S2 sample), a second doublet appears at 464.6 and 458.9 eV, with values closer to those found for anatase-like TiO_2 materials.[49,50] However, the $Ti2p_{3/2}$ peak still presents a significant deviation from TiO_2-SA (458.9 against 458.5 eV). Thus, for that sample, distorted octahedral Ti species coexist with very small TiO_2 nanoparticles interacting strongly with the support (see STEM discussion). For higher TiO_2 content (30 and 50 wt%), the spectra are dominated by a doublet at 464.2 and 458.5 eV, typical of bulk TiO_2 oxide. However, the Ti2p spectra of the S1 series samples are very similar to bulk TiO_2-SA (see Fig. S7†), which shows that polymeric TiO_2 species are present in these samples.

The XPS spectra corresponding to the O1s region (Fig. 9, right) corroborate the previous conclusions well. HBEA support shows a main O1s signal at 532.3 eV attributed to Si–O–Si groups and two others, but less intense peaks at 531.1 and 533.2 eV, corresponding to Si–O–Al/Si–OH and H_2O species, respectively.[51] When Ti is introduced ($10TiO_2$-BEA S2 sample), the band at 531.1 eV increases in intensity and shifts to 531.7 eV, while another band appears at 530.0 eV. Because the Si/Al ratio of the starting BEA support did not change with the introduction of Ti, the increase in the band at *ca.* 531.7 eV may be attributed to the Si–O–Ti groups, which were formed during the incorporation of Ti. The band appearing at a lower binding energy is attributed to the Ti–O groups. The appearance of these two bands agrees well with the formation of hexacoordinated TiO_6 species, strongly attached to the zeolite support. With the further increase in Ti content in the composites, the band associated with Ti–O groups now dominates the O1s spectra, while the bands ascribed to Si–O–Si and Si–O–Ti species decrease in intensity although maintaining the same relative intensity. For these two samples, 30 and $50TiO_2$-BEA S2, the main TiO_2 species can now be regarded as anatase-like TiO_2 species.

Table 3 Chemical analysis of the different composites obtained from EDS and XPS analyses

		Si/Al	Si/Ti	Si/Al	Si/Ti
Sample	Si/Ti	EDS analysis		XPS analysis	
H-BEA	0	—	—	12.7	—
$20TiO_2$-BEA S1	4.9	11.4	4.9	nd	nd
$30TiO_2$-BEA S1	2.9	8.7	1.8	nd	nd
$10TiO_2$-BEA S2	11.1	10.8	9.8	12.0	3.2
$20TiO_2$-BEA S2	4.9	11.3	4.8	9.3	1.1
$30TiO_2$-BEA S2	2.9	11.3	2.4	9.7	0.7
$50TiO_2$-BEA S2	1.2	10.6	1.9	5.4	0.2

nd – not determined.

Table 3 presents the results of the chemical analysis of the different composites. The experimental Si/Al and Si/Ti ratios determined from both the EDS and XPS analyses are presented together with the theoretical values. In the case of EDS analysis, the experimental results fairly agree with the theoretical ones for both Si/Al and Si/Ti ratios. As the composites are essentially composed of very small nanoparticles (20–40 nm), one can consider this EDS analysis a bulk analysis. However, XPS analysis is well known for providing information about the surface of the material. In this case, the experimental results differ significantly from the theoretical ones. For example, the experimental Si/Al ratio determined by XPS decreases with the amount of TiO_2 in the final materials. This observation could be explained by the fact that the Si signal is more attenuated than the Al one.[52] More interestingly, the experimental Si/Ti ratio is significantly lower than the expected one, which shows enrichment of Ti species at the surface of the composites compared with the bulk, in agreement with the aforementioned results.

Evaluation of the performance of the TiO_2-BEA composites in the photooxidation of ethylene

To analyse the advantages of TiO_2-based zeolite composites compared with bulk TiO_2, we analysed, in a first approach, the comparative performance under UV-vis radiation of the H-BEA support, the bulk TiO_2-S2 sample and also the composite with intermediate TiO_2 loading ($20TiO_2$-BEA S2), considering that TiO_2 is expected to be only active under UV-radiation. Moreover, because the samples possess an important porosity, to avoid any contribution of ethylene adsorption to the final conversion of the photocatalysts, all the samples were previously saturated in the dark. The corresponding breakthrough curves were recorded and allowed to determine the ethylene adsorption capacity of each sample (see Fig. 10). As expected, the porous support H-BEA shows an ethylene adsorption of about 13 μmol g^{-1}, while the adsorption can be considered negligible for the bulk TiO_2 sample. However, the $20TiO_2$-BEA S2 sample

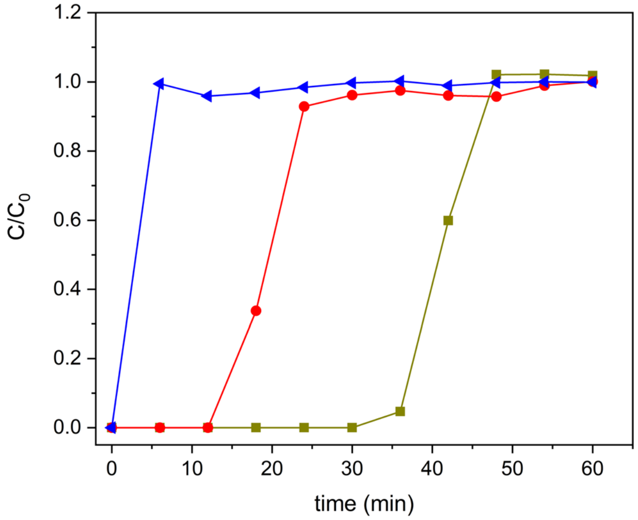

Fig. 10 Ethylene adsorption curves for samples H-BEA (■), 20TiO$_2$-BEA S2 (●) and TiO$_2$-S2 (◀) (C_2H_4 100 ppm, 25 cm^3 min^{-1}, RT).

presents an intermediate ethylene adsorption capacity, with a value of 5 μmol g^{-1}, due to the blockage of the support porosity. This result demonstrates the advantage of using a support such as zeolite, concentrating the ethylene close to the TiO$_2$ photoactive species.

After saturation in the dark, the UV lamp is lighted on, and the photocatalytic reaction can proceed. The results obtained are shown in Fig. 11. Pristine zeolite support does not show any photocatalytic activity. However, both 20TiO$_2$-BEA S2 and TiO$_2$-S2 samples convert completely ethylene, with 100% selectivity to CO$_2$. These results confirm that the composites selectively remove all the ethylene present in the gas stream. However, the pre-concentration of ethylene on the catalyst's surface makes the CO$_2$ concentration profiles different for the two samples. The composite material presents a huge CO$_2$ peak at the beginning of the experiment, which is not present for the bulk TiO$_2$-S2 sample. This peak is due to the combustion of the pre-adsorbed ethylene on the composite during the adsorption step in the dark,[53] indicating the beneficial effect of zeolite support in concentrating ethylene.

As mentioned above, although 20TiO$_2$-BEA S2 presents a lower TiO$_2$ amount when compared with the TiO$_2$-S2 sample, the photocatalyst can still completely convert ethylene. This result clearly shows the advantages of using a zeolite-based photocatalytic material. The UV results concerning the other composites can be found in the ESI† (Fig. S8). Nonetheless, from the viewpoint of the economy and sustainability of the processes, the great challenge is to improve the performance of TiO$_2$ under visible (solar) light regarding artificial UV light. Thus, after demonstrating good performance under UV, the different composites were compared under UVA-vis radiation. The results are presented in Fig. 12. It is noteworthy that these photocatalytic results have been obtained under dynamic gas-phase conditions, which could present high interest in photocatalytic oxidation applications.[5]

The efficiency of the photooxidation process decreased under UVA-vis irradiation. This lower photocatalytic performance can be explained by the smaller energy of the radiation but also by the fact that the samples present a lower absorption in the UV-vis range (Fig. 7), which limits the excitation of the active sites. This fact is notorious for all the samples and, in particular, for the S2 sample. However, when comparing the performance of the different samples (Fig. 12), the composite prepared under a basic medium presents a higher ethylene conversion when compared with its counterparts obtained under an acidic medium. As expected, the conversion increased with increasing TiO$_2$ loadings from 20 to 30 wt% in the S1 series. Nevertheless, the 20TiO$_2$-BEA S2 sample maintained a high performance, even better than

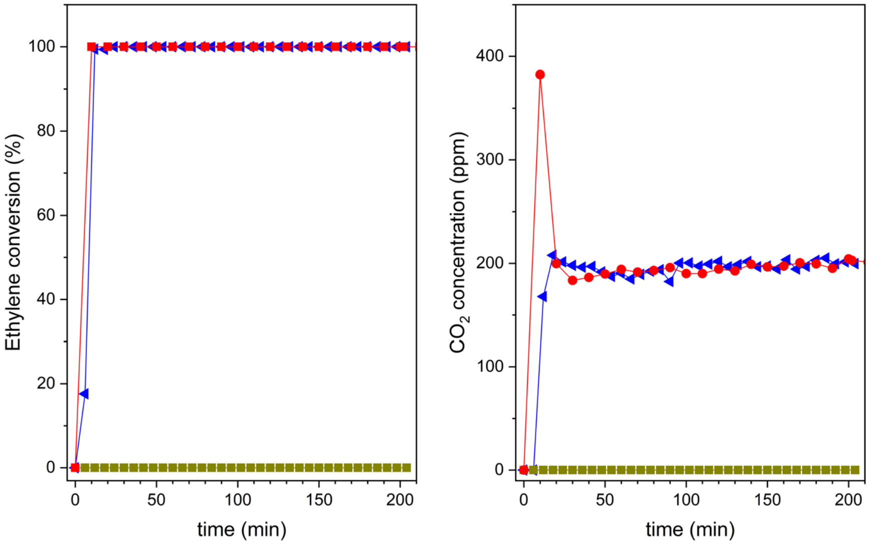

Fig. 11 Ethylene photooxidation experiments under UV-vis light for H-BEA (■), 20TiO$_2$-BEA S2 (●) and TiO$_2$-S2 (◀): (left) ethylene conversion; (right) CO$_2$ concentration (experimental conditions C_2H_4 100 ppm, 25 cm^3 min^{-1}, 0.45 g).

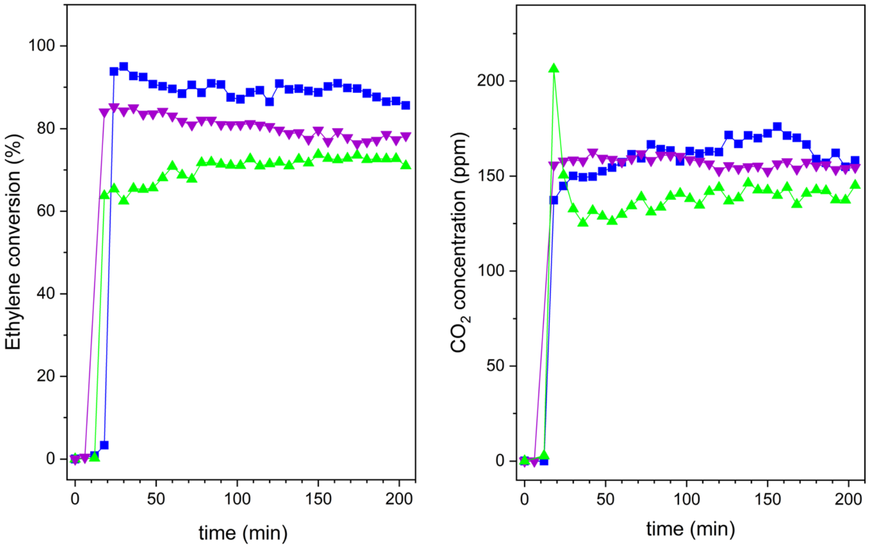

Fig. 12 Ethylene photooxidation experiments under UVA-vis irradiation for 20TiO_2-BEA S2 (■); 20TiO_2-BEA S1 (▲) and 30TiO_2-BEA S1 (▼): (left) ethylene conversion; (right) CO_2 concentration (experimental conditions C_2H_4 100 ppm, 25 cm^3 min^{-1}, 0.45 g).

30TiO_2-BEA S1, but without reaching 100% conversion, as the samples demonstrated in the previous UV experiments.

Therefore, the following results, depicted in Fig. 13, only concern the influence of the TiO_2 concentration on the photocatalytic performance of the S2 series samples. In this case, the reference material TiO_2-S2 was also included for comparison. As it was already observed for the S1 series samples, here we can observe that the ethylene conversion also increases with the TiO_2 loading, and samples with a TiO_2 wt% of 30 or higher show a 100% conversion of ethylene, as the bulk TiO_2-S2 sample does. The crystallization of isolated TiO_2 nanoparticles (see the SEM results) might contribute to this total ethylene conversion. However, CO_2 is always the only product of the reaction, as confirmed by the carbon balance. As shown in Fig. 11, one of the differences in performance between composites and pure TiO_2 is the capacity of the former to oxidize ethylene molecules previously adsorbed. Under UV-radiation, this occurs for sample 20TiO_2-BEA S2 but not under vis-radiation (Fig. 13B) or for sample 10TiO_2-BEA S2. This oxidation of pre-adsorbed ethylene occurs only for the samples with higher TiO_2 loadings, such as 30 and 50TiO_2-BEA S2 ones. As ethylene adsorption should decrease with increasing TiO_2 loadings (because the porosity of the composites decreases), this difference in behaviour might reveal a difference in nature of the active sites, with low TiO_2 composites clearly inactive for the oxidation of pre-adsorbed ethylene, as no CO_2 peaks at the reaction beginning can be observed. These results agree with the XPS results, which show a clear difference in the nature of the active sites between samples with low and high loadings. Logically, the bulk TiO_2-S2 sample does not show any CO_2 peak at the beginning of the experiment, as it shows no ethylene adsorption capacity (see Fig. 13B).

To understand the reactivity of the different active sites on the composites, the results were expressed and compared in terms of TOF for the 10 and 20TiO_2-BEA S2 samples, as higher loadings lead to total conversion and thus cannot be compared (see Fig. 13C and D). Although the samples present very different conversion values, the activity for both composites is very similar after 3 h on stream (TOF of about 1.10^{-6} s^{-1}). Clearly, the photocatalytic sites seem to be more active at low loading although they seem to undergo significant deactivation, which could occur also, to a lesser extent, for sample 20TiO_2-BEA S2. Curiously, while the profile of either TOF or ethylene conversion decreased with time on stream for the samples with lower loadings, the formation of CO_2 increased (Fig. 13D). This is a consequence of some ethylene pre-adsorbed in these samples and not oxidized but that desorbs under radiation because the light is not powerful enough to oxidize the species but only to desorb it, decreasing the ethylene conversion values. This means that the deactivation observed is only apparent. With the ethylene being desorbed, the freshly free active sites can interact with additional ethylene molecules or activate O_2 to produce peroxide radicals, which, in turn, oxidize the ethylene molecules. Additional experiments are required to address this question, in order to elucidate the reaction mechanisms involved (Langmuir–Hinshelwood or Eley–Rideal) and to better define the correlation between the different photoactive sites.

Nevertheless, one can see that the TiO_2-BEA composites demonstrate excellent performance in the photooxidation of ethylene although with a lower amount of TiO_2 when compared with bulk TiO_2 materials. Here, the zeolite support seems to be a key point in the excellent photocatalytic performance of the nanocomposites, acting in distinct ways: a) by allowing good dispersion and accessibility of the TiO_2 photoactive phase, namely both isolated TiO_2 species and TiO_2 nanoparticles, b) by gathering and concentrating ethylene molecules close to the photoactive sites and c) by limiting or delaying the recombination of the electron–hole

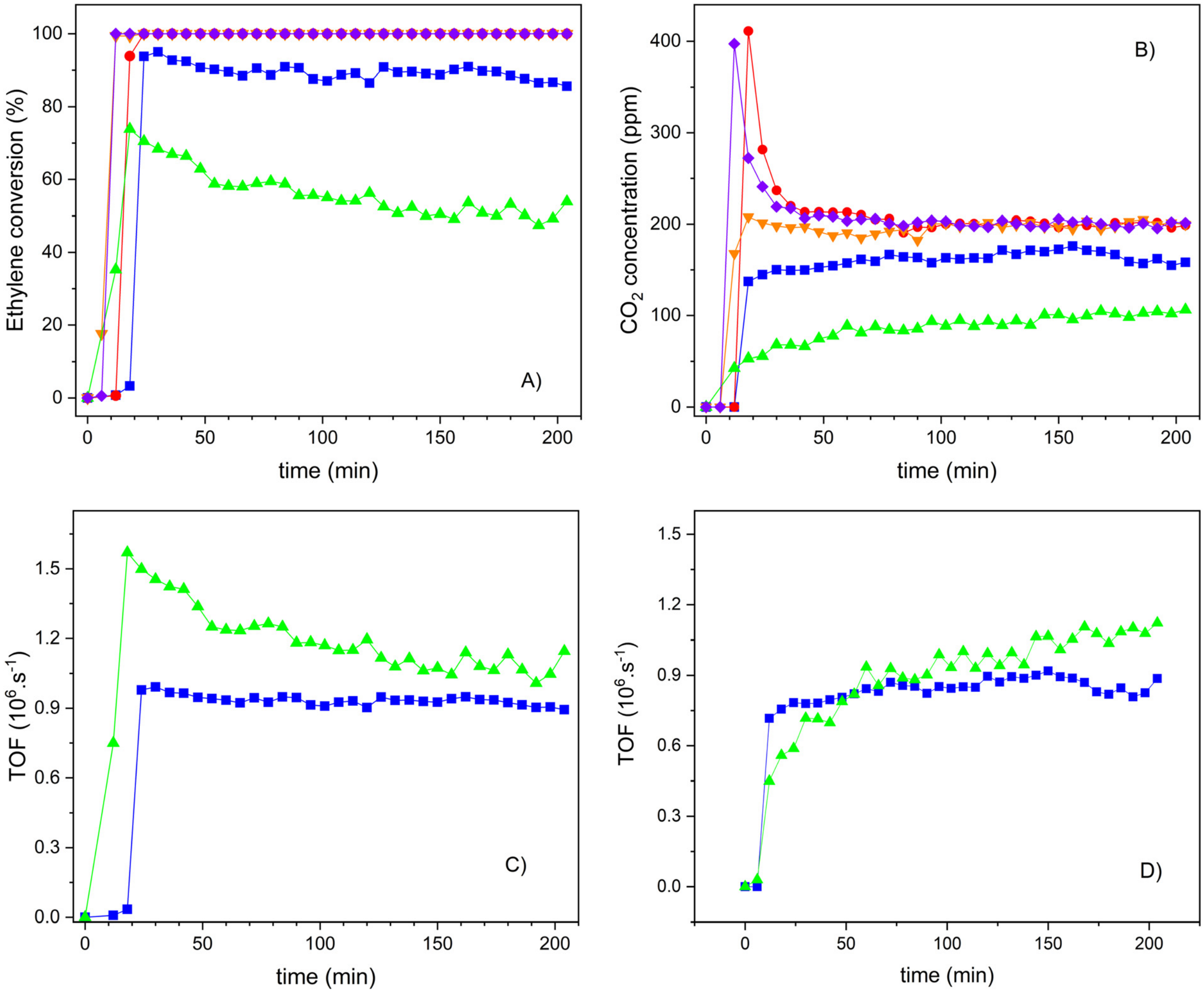

Fig. 13 Ethylene photooxidation experiments under UVA-vis irradiation for S2 series samples: A) ethylene conversion; B) CO_2 concentration; C) TOF values (calculated from ethylene); and D) TOF values (calculated from CO_2) (10TiO$_2$-BEA S2 (▲), 20TiO$_2$-BEA S2 (■), 30TiO$_2$-BEA S2 (●), 50TiO$_2$-BEA S2 (◆) and TiO$_2$-S2 (▼); experimental conditions: C_2H_4 100 ppm, 25 cm^3 min^{-1}, 0.45 g).

pairs, a paramount parameter for the photodegradation process (see Scheme 1).

Experimental

Materials and methods

Commercial zeolite parent (NH_4-BEA, Si/Al of 12.5, *i.e.* CP814E) was purchased from Zeolyst. Titanium isopropoxide (97% w/w) and titanium dioxide (TiO_2-SA) were purchased from Sigma Aldrich. HNO_3 (65% w/w) was purchased from Panreac, NH_4OH (25% NH_3) was obtained from Fluka, and ethanol absolute (99.5% w/w) and 2-propanol (99.8% w/w) were both supplied by Honeywell.

Preparation of TiO$_2$/BEA composites

TiO_2/BEA composites were prepared by applying the sol–gel method, using two distinct approaches combining different solvents and catalysts: 2-propanol/HNO_3 and ethanol/NH_4OH. Samples prepared under acidic or basic medium are denoted as S1 or S2, respectively.

Method S1 (2-propanol/HNO$_3$). 1.5 g of BEA zeolite is suspended in a 2-propanol solution (20 ml) containing the titanium precursor (Ti[OCH(CH$_3$)$_2$]$_4$), and the mixture is stirred for 2 h. After that, an aqueous solution of HNO_3 (20 mL, 0.5 M) is added dropwise. Then, the suspension is stirred for 2 additional hours. Finally, the suspension is dried using a rotatory evaporator (Buchi Rotavapor R-210). The powder is finally recovered, ground, and calcined in a muffle at 450 °C for 4 h (2 °C min^{-1} heating rate).

Method S2 (ethanol/NH$_4$OH). 1.5 g of BEA zeolite is suspended in an ethanol solution (15 ml) containing the titanium precursor (Ti[OCH(CH$_3$)$_2$]$_4$), and the mixture is stirred for 15 min. Then, an ammonium hydroxide solution (NH_4OH, ∼25% in water) (20 mL, 1 M) is added dropwise. The suspension is then stirred for 3 h. Finally, the suspension is dried using a rotatory evaporator, and the powder is recovered, ground and calcined in a muffle at 450 °C for 4 h (2 °C min^{-1} heating rate).

For both methods, by changing the initial amount of Ti precursor in the alcoholic solution, BEA samples with 20–30

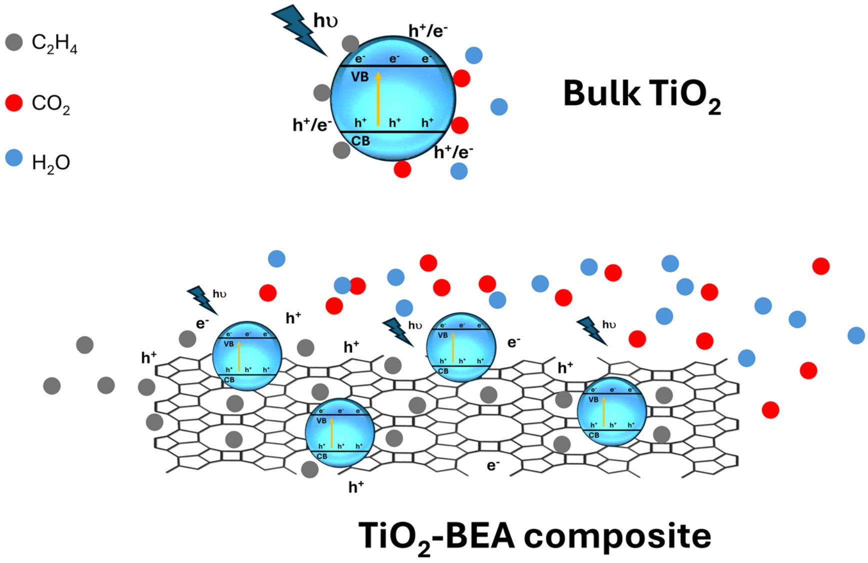

Scheme 1 Illustration of the adsorption and the photocatalytic degradation of ethylene on the surface of bulk TiO_2 *vs.* zeolite-based TiO_2 composites.

wt% (S1 method) or 10–50 wt% TiO_2 (S2 method) are obtained. Moreover, for comparison, 2 TiO_2 bulk reference samples, using the same sol–gel methods but without zeolite, were also prepared (TiO_2-S1 and TiO_2-S2). TiO_2/BEA composites are named as follows: xTiO₂-BEA SI, where x represents the amount of TiO_2 (wt%) and SI represents the method used (S1 for 2-propanol/HNO_3 and S2 for ethanol/NH_4OH, respectively). Table 4 lists all the samples prepared for the ethylene photooxidation experiments.

Composite characterization

The composites were characterized by different techniques. Powder X-ray diffraction patterns were recorded using a D8 Advance diffractometer (Bruker) with Cu Kα radiation filtered by Ni and a 1D LynxEye detector. Quantitative phase analysis and crystallite size measurements were performed by applying the Rietveld/whole pattern fitting method (fundamental parameters approach) with TOPAS V.5 software from Bruker AXS. Nitrogen sorption experiments were performed using Autosorb IQ equipment from Quantachrome. Before each measurement, the samples were outgassed first at 90 °C and then at 350 °C for 1 and 5 h, respectively. DRS UV-visible spectra were recorded using a Praying Mantis diffuse reflectance accessory coupled to a Cary 5000 spectrophotometer (Varian). The band gap (E_g) of the different materials was calculated from the corresponding Tauc plots (indirect method[54]). X-ray photoelectron spectroscopy (XPS) was carried out using a Physical Electronics VersaProbe II apparatus with a MgKα X-ray source ($h\nu$ = 1486.6 eV) working at 1.3 eV and 20 mA, and a hemispherical electron analyser. Infrared spectra (KBr method) were obtained in transmission mode, with pellets consisting of samples diluted with KBr (0.5 wt%). Pyridine adsorption, followed by FTIR, was performed in line with previous work.[55] The following molar extinction coefficients, determined in our IR setup, were used (ε_B = 0.91 and ε_L = 1.58 cm μmol^{-1}, for Brønsted and Lewis acid sites at 1545 and 1455–45 cm^{-1}). A Thermo Nicolet Nexus 960 spectrometer was used in both cases. Raman spectra were collected using Labram HR 800 Evolution equipment from Horiba, Jobin Yvon. Spectra were obtained with a 532 nm excitation source and a laser power of *ca.* 10 mW. Data were collected for 10 s and 4 accumulations using a 100× objective lens. SEM images were acquired using a Hitachi Regulus 8220 Scanning Electron Microscope equipped with an energy dispersive X-ray spectrometer (EDS) from Oxford Instruments. Scanning Transmission Electron Microscopy (STEM) analyses, including High-Angle Annular Dark-Field (HAADF) imaging, were carried out using a Hitachi HF5000 field-emission transmission electron microscope operating at 200 kV equipped with a 100 mm^2 EDS detector from Oxford Instruments. A drop of the sonicated dispersions was applied to the lacey-carbon copper grids and left to dry prior to STEM observation.

Table 4 Summary of all the composites prepared, alcohol used and TiO_2 concentration

Sample	Alcohol	Catalyst	TiO_2 (wt%)
HBEA	—	—	—
20TiO_2-BEA S1	2-Propanol	HNO_3	20
30TiO_2-BEA S1	2-Propanol	HNO_3	30
TiO_2-S1	2-Propanol	HNO_3	100
10TiO_2-BEA S2	Ethanol	NH_4OH	10
20TiO_2-BEA S2	Ethanol	NH_4OH	20
30TiO_2-BEA S2	Ethanol	NH_4OH	30
50TiO_2-BEA S2	Ethanol	NH_4OH	50
TiO_2-S2	Ethanol	NH_4OH	100

Ethylene adsorption and photodegradation experiments

The experimental setup utilized was the same one used by Regadera-Macías *et al.*[53] Before ethylene photodegradation experiments, samples are pre-treated in a muffle at 250 °C for 25 min to clean up the surface of the materials. Composites are then loaded into a quartz reactor (0.45 g) operating at atmospheric pressure. A total flow of 25 cm^3 min^{-1} was used with the following mixture of gases (100 ppm C_2H_4/He 5%/O_2 21%, N_2). Before each photocatalytic experiment, the gas mixture is allowed to pass through the sample under the dark to reach ethylene adsorption equilibrium; the corresponding breakthrough curves are recorded and properly analysed. The sample is then irradiated with a medium-pressure mercury lamp equipped with a cooling jacket (irradiation spectrum is shown in Fig. S9, ESI†). Depending on the cooling jacket material used, quartz, or glass, experiments can be conducted under UV-vis or UVA-vis illumination, respectively. The glass jacket completely removes the radiation for $\lambda < 300$ nm, while the UVA-vis radiation with $\lambda > 350$ nm corresponds to 74% of the lamp irradiation power. The total time for each reaction was 3 h and 30 min.

Conclusions

This study reports the use of two different sol–gel methods for the preparation of photocatalytic TiO_2-based zeolite (BEA) composites. The main idea here is to prepare photoactive composites that are highly efficient for the photodegradation of ethylene and can integrate photocatalytic devices to control ethylene in industrial cold storage facilities. The two synthesis strategies changed when using either an acidic or a basic medium during the sol–gel preparation of the TiO_2 nanoparticles, as the zeolite support was introduced before the titanium precursor hydrolysis step. The two synthesis strategies resulted in photocatalytic composites with distinct properties. For the samples prepared under an acidic medium, the isolated TiO_2 nanoplatelets crystallized separately from the zeolite support. However, for the samples obtained under basic conditions, a stronger interaction between the growing TiO_2 nanoparticles and the zeolite support was found, leading to highly dispersed TiO_2 nanoparticles over the BEA zeolite support. Moreover, the resulting photocatalytic composites demonstrated excellent performance in the photooxidation of ethylene, despite a rather low amount of TiO_2 when compared with bulk TiO_2 material, prepared without the zeolite support and used as photocatalytic reference. Here, the BEA support was shown to be decisive in the excellent photocatalytic performance of the nanocomposites, as the zeolite support might exhibit different but distinct roles in: a) allowing a good dispersion and accessibility of the TiO_2 photoactive phase, namely both isolated TiO_2 species and TiO_2 nanoparticles, b) gathering and concentrating ethylene molecules close to the photoactive sites and c) limiting or delaying the electron–hole pair recombination, a paramount parameter for the photodegradation process. Finally, photocatalysis might be a really promising ethylene removal technology capable of competing with the conventional technologies currently used in industrial cold storage facilities. However, significant efforts must be made to reach a level of technology that is as mature as those found in indoor air treatments. This means a great effort in what concerns the design and engineering of photoreactors. Our TiO_2-BEA photocatalysts, tested under continuous gas-phase conditions, have proven to be good candidates for this purpose.

Data availability

The data supporting this article have been included as part of the ESI.†

Author contributions

R. F.: writing – original draft; investigation; S. M. T.: methodology, data curation, writing – review & editing, supervision; L. M. P. M.: data curation, formal analysis, writing – review & editing, supervision. F. J. M. H.: conceptualization, validation; resources, project administration, funding acquisition, writing – review & editing, supervision; J. P. L.: conceptualization, writing – review & editing; J. M. S.: writing – review & editing; I. M. J.: writing – review & editing; M. F. R.: conceptualization, resources, project administration, funding acquisition, writing – review & editing; supervision; A. F.: conceptualization, investigation, writing – review& editing, supervision.

Conflicts of interest

There are no conflicts to declare.

Acknowledgements

The authors thank FCT for providing funding through projects Nano4fresh-PRIMA/0015/2019 (**http://doi.org/10.54499/PRIMA/0015/2019**), UIDB/00100/2020 (CQE) (**https://doi.org/10.54499/UIDB/00100/2020**), UIDP/00100/2020 (CQE) (**https://doi.org/10.54499/UIDP/00100/2020**), UIDB/00097/2020 (CEGIST) (**https://doi.org/10.54499/UIDB/00097/2020**) and LA/P/0056/2020 (IMS) (**https://doi.org/10.54499/LA/P/0056/2020**), project PCI2020-112045 from MCIN/AEI/10.13039/501100011033 and European Union Next Generation EU/PRTR; and partially by projects PID2021-126579OB-C31 funded through MCIN/AEI/10.13039/501100011033 and "ERDF A way of making Europe"; P21_00208 from Consejería de Universidad, Investigación e Innovación – Junta de Andalucía. SMT is grateful to MCIN/AEI/10.13039/501100011033 and the European Social Found (FSE) "El FSE invierte en tu futuro" for a Ramon y Cajal research contract (RYC-2019-026634-I). A. F. thanks Instituto Superior Técnico for the Scientific Employment contract under law DL 57/2016. R. Ferreira also thanks FCT for the PhD grant (2022.12593.BD).

Notes and references

1 M. H. Álvarez-Hernández, F. Artés-Hernández, F. Ávalos-Belmontes, M. A. Castillo-Campohermoso, J. C. Contreras-Esquivel, J. M. Ventura-Sobrevilla and G. B. Martínez-Hernández, *Food Bioprocess Technol.*, 2018, **11**, 511–525.

2 S. Anand and M. K. Barua, *Comput. Electron. Agric.*, 2022, **198**, 106936.

3 *Controlled Atmosphere Storage of Fruit and Vegetables*, ed. A. K. Thompson, R. K. Prange, R. D. Bancroft and T. Puttongsiri, CABI, 3rd edn, 2018.

4 H. Wei, F. Seidi, T. Zhang, Y. Jin and H. Xiao, *Food Chem.*, 2021, **337**, 127750.

5 N. Keller, M.-N. Ducamp, D. Robert and V. Keller, *Chem. Rev.*, 2013, **113**, 5029–5070.

6 N. Pathak and P. Mahajan, in *Reference Module in Food Science*, Elsevier, 2017.

7 Q. Zhang, G. Xie, M. Duan, Y. Liu, Y. Cai, M. Xu, K. Zhao, H. Tai, Y. Jiang and Y. Su, *ACS Appl. Nano Mater.*, 2023, **6**, 17445–17456.

8 K. Hashimoto, H. Irie and A. Fujishima, *Jpn. J. Appl. Phys.*, 2005, **44**, 8269.

9 W. Zhang and J.-W. Rhim, *Food Packag. Shelf Life*, 2022, **31**, 100806.

10 J. de M. Fonseca, M. J. dos S. Alves, L. S. Soares, R. de F. P. M. Moreira, G. A. Valencia and A. R. Monteiro, *Food Res. Int.*, 2021, **144**, 110378.

11 Q. Sun, N. Wang and J. Yu, *Adv. Mater.*, 2021, **33**, 2104442.

12 G. Bellussi and R. Millini, in *Structure and Reactivity of Metals in Zeolite Materials*, ed. J. Pérez Pariente and M. Sánchez-Sánchez, Springer International Publishing, Cham, 2018, pp. 1–52.

13 Y. Xu and C. H. Langford, *J. Phys. Chem. B*, 1997, **101**, 3115–3121.

14 M. Lafjah, F. Djafri, A. Bengueddach, N. Keller and V. Keller, *J. Hazard. Mater.*, 2011, **186**, 1218–1225.

15 M. Anpo and M. Takeuchi, *J. Catal.*, 2003, **216**, 505–516.

16 X. Liang, X. Peng, C. Xia, H. Yuan, K. Zou, K. Huang, M. Lin, B. Zhu, Y. Luo and X. Shu, *Ind. Eng. Chem. Res.*, 2021, **60**, 1219–1230.

17 Z. Yang, Q. Yu, Y. Guo, X. Wu, H. Wang, J. Han, Q. Ge and X. Zhu, *Microporous Mesoporous Mater.*, 2022, **330**, 111625.

18 M. Mahalakshmi, S. Vishnu Priya, B. Arabindoo, M. Palanichamy and V. Murugesan, *J. Hazard. Mater.*, 2009, **161**, 336–343.

19 J. Fernández-Catalá, M. Sánchez-Rubio, M. Navlani-García, Á. Berenguer-Murcia and D. Cazorla-Amorós, *ACS Omega*, 2020, **5**, 31323–31331.

20 M. El-Roz, L. Lakiss, J. El Fallah, O. I. Lebedev, F. Thibault-Starzyk and V. Valtchev, *Phys. Chem. Chem. Phys.*, 2013, **15**, 16198–16207.

21 A. Molea, V. Popescu, N. A. Rowson and A. M. Dinescu, *Powder Technol.*, 2014, **253**, 22–28.

22 S. T. Aruna, S. Tirosh and A. Zaban, *J. Mater. Chem.*, 2000, **10**, 2388–2391.

23 M. Bahar, M. Mozaffari and S. Esmaeili, *J. Theor. Appl. Phys.*, 2017, **11**, 79–86.

24 A. Indekeu, E. Bailón-García, A. Fernandes, R. Baltazar, A. M. Ferraria, A. M. B. do Rego and M. Filipa Ribeiro, *Catal. Today*, 2021, **379**, 272–284.

25 T. Ohno, K. Sarukawa, K. Tokieda and M. Matsumura, *J. Catal.*, 2001, **203**, 82–86.

26 A. Bahramian, *Ind. Eng. Chem. Res.*, 2013, **52**, 14837–14846.

27 F. Geobaldo, S. Bordiga, A. Zecchina, E. Giamello, G. Leofanti and G. Petrini, *Catal. Lett.*, 1992, **16**, 109–115.

28 J. Klaas, G. Schulz-Ekloff and N. I. Jaeger, *J. Phys. Chem. B*, 1997, **101**, 1305–1311.

29 A. F. Silva, A. Fernandes, P. Neves, M. M. Antunes, S. M. Rocha, M. F. Ribeiro, C. M. Silva and A. A. Valente, *ChemCatChem*, 2018, **10**, 2741–2754.

30 Y. Kissoum, D. E. Mekki, M. Bououdina, E. Sakher and S. Bellucci, *J. Supercond. Novel Magn.*, 2020, **33**, 427–440.

31 E. M. Flanigen, H. Khatami and H. A. Szymanski, in *Molecular Sieve Zeolites-I*, American Chemical Society, 1974, vol. 101, pp. 16–201.

32 H. Chen, A. Matsumoto, N. Nishimiya and K. Tsutsumi, *Colloids Surf., A*, 1999, **157**, 295–305.

33 S. Zheng, L. Gao, Q. Zhang and J. Guo, *J. Mater. Chem.*, 2000, **10**, 723–727.

34 Y. Xu and C. H. Langford, *J. Phys. Chem.*, 1995, **99**, 11501–11507.

35 P. K. Doolin, S. Alerasool, D. J. Zalewski and J. F. Hoffman, *Catal. Lett.*, 1994, **25**, 209–223.

36 C. U. Ingemar Odenbrand, J. G. M. Brandin and G. Busca, *J. Catal.*, 1992, **135**, 505–517.

37 C. U. Ingemar Odenbrand, S. Lars, T. Andersson, L. A. H. Andersson, J. G. M. Brandin and G. Busca, *J. Catal.*, 1990, **125**, 541–553.

38 S. Yamazaki, S. Tanaka and H. Tsukamoto, *J. Photochem. Photobiol., A*, 1999, **121**, 55–61.

39 M. V. P. Sharma, V. Durgakumari and M. Subrahmanyam, *J. Hazard. Mater.*, 2008, **160**, 568–575.

40 N. Hoeven, G. Mali, M. Mertens and P. Cool, *Microporous Mesoporous Mater.*, 2019, **288**, 109588.

41 V. Durgakumari, M. Subrahmanyam, K. V. Subba Rao, A. Ratnamala, M. Noorjahan and K. Tanaka, *Appl. Catal., A*, 2002, **234**, 155–165.

42 M. El-Roz, P. Bazin and F. Thibault-Starzyk, *Catal. Today*, 2013, **205**, 111–119.

43 P.-P. Knops-Gerrits, D. E. De Vos, E. J. P. Feijen and P. A. Jacobs, *Microporous Mater.*, 1997, **8**, 3–17.

44 H. She, G. Ding, X. Li, H. Wang, D. Cao, Y. Zhu and Y. Li, *J. Fuel Chem. Technol.*, 2021, **49**, 1148–1160.

45 D. T. On, L. Bonneviot, A. Bittar, A. Sayari and S. Kaliaguine, *J. Mol. Catal.*, 1992, **74**, 233–246.

46 M. A. Camblor, A. Corma, A. Martínez and J. Pérez-Pariente, *J. Chem. Soc., Chem. Commun.*, 1992, 589–590.

47 T. Blasco, M. A. Camblor, A. Corma and J. Perez-Pariente, *J. Am. Chem. Soc.*, 1993, **115**, 11806–11813.

48 T. Blasco, M. A. Camblor, J. L. G. Fierro and J. Pérez-Pariente, *Microporous Mater.*, 1994, **3**, 259–263.

49 S. Praserthdam, M. Rittiruam, K. Maungthong, T. Saelee, S. Somdee and P. Praserthdam, *Sci. Rep.*, 2020, **10**, 18952.

50 G. I. Supelano, F. Mesa, C. A. P. Vargas, J. A. M. Gómez and A. Dussan, *Sci. Rep.*, 2023, **13**, 3650.

51 A. Walkowiak, L. Wolski and M. Ziolek, *Molecules*, 2020, **25**(24), 5781.

52 J. Matthew, *Surf. Interface Anal.*, 2004, **36**, 1647.

53 A. M. Regadera-Macías, S. Morales-Torres, L. M. Pastrana-Martínez and F. J. Maldonado-Hódar, *Catal. Today*, 2023, **413–415**, 113932.

54 P. Makuła, M. Pacia and W. Macyk, *J. Phys. Chem. Lett.*, 2018, **9**, 6814–6817.

55 J. M. Silva, M. F. Ribeiro, I. Graça and A. Fernandes, *Microporous Mesoporous Mater.*, 2021, **323**, 111170.